Additive Manufacturing of Locally Weakened Parts to Obtain a Designed Fracture

Manuela Galati[1] · Silvio Defanti[2]

Abstract

Today, the additive manufacturing (AM) approach has led to profound changes in part and process design, enabling previously impossible material properties. With the freedom to create the material as components are built layer by layer, AM has permitted precise spatial control of the material properties in manufactured parts. In this work, an original approach is proposed to locally control component and process design and create intentionally weakened regions with designed fracture, which paves the way to tuneable mechanical properties. Tensile tests of specimens with embedded weakened area of various geometries are used to verify the feasibility of a-priori-designed fracture modes and to characterise the variation in material behaviour. The results show that an ad hoc design of the artificially weakened areas is effective for predictable breakage, with load and strain being the precursor for active control of the mechanical behaviour. The attainability of a quantitative relationship between the defect and the mechanical response is exemplified by the fact that, e.g. for a flat geometry, the maximum stress and strain are reduced by half when the thickness of the weak region is doubled.

1 Introduction

The additive manufacturing (AM) approach is characterised by the unique ability to create the material while the component is being built [1]. The process nature of AM enables producing parts with high material and design complexity [2]. The 3D spatial control of the process at different length scales introduces new additional parameters and allows local tuning of material properties [3]. This principle finds application in the fabrication of site-specific properties in functionally graded materials (FGMs) [4], tailored physical properties or material distribution in composite structures [5], and in-situ alloying for spatial modulation of the composition [6]. It is well known that the concurrent design of the component geometry and a favourable microstructure leads to optimised component behaviour [7], generally in terms of superior mechanical properties [8]. AM is particularly suitable for modifying part properties, e.g. mechanical ones, by varying the process parameters or changing the microstructure [9, 10] through subsequent post-processing, such as heat treatments [11]. Similarly, layered manufacturing enables design with complex geometric variations to regulate component performance. Examples of using design to control and achieve specific properties include metamaterials [12–14], commonly referred to as lattice structures used extensively in biomedical applications [15]. In all these cases, the optimisation of the process aims at obtaining a fully-densified structure in all sections of the component [7], avoiding any defects such as lack of fusion [7] or cracks [16]. An alternative approach is taken by Min et al. [17], who studied the relationship between porosity and elasticity in pure titanium with a view to conversion to porous load-bearing implants. Variations in material density can significantly alter the mechanical behaviour of a part, as well as its thermal, electrical and magnetic properties[18]. If the non-uniform density is intentionally designed and controlled, localised porosities can be useful to achieve a specific behaviour [19]. A similar concept was investigated by Pedersen [20], who calculated that, in a continuous part,

✉ Manuela Galati
manuela.galati@polito.it

1 Department of Management and Production Engineering, Politecnico di Torino, Torino, Italy

2 Department of Engineering 'Enzo Ferrari', University of Modena and Reggio Emilia, Modena, Italy

the proper coexistence of two materials, one of which is a weakening of the other, could significantly minimize the internal resonances of the system. With a completely different goal, Maucher et al. [21] adjusted the AM process parameters to produce a machining allowance with lower strength and easier machinability.

In complex systems consisting of many components, control of mechanical resistance and component failure can play a fundamental role. If the system is overloaded or operates outside the safety load range, unpredictable failure can occur in any part of the structure, resulting in irreparable damage and safety hazards. Mechanisms whose deformation or rupture are controlled can prevent such catastrophic failure of the entire system. Devices that integrate controlled deformation mechanisms are already in use. Examples are the fuses for seismic applications [22] and Cardan shafts [23]. On the other hand, the possibility of controlling the fracture of a product has also found more exotic applications, such as mouthfeel control using edible mechanical metamaterials [24]. In all these cases, the expected deformation and fracture mechanisms are achieved by acting on the component geometry.

This paper builds on an original procedure for designing and fabricating components in which the external geometry remains uniform, while inner portions, with ad-hoc design are not fully densified. The innovative procedure allows a design of the fracture areas under stress and tracing preferential paths within the product for thermal and electrical fluxes. The method was described in a recent patent application [25]. This paper reports the experimental validation of this method applied to the tensile behaviour and fracture mode of Ti6Al4V specimens fabricated using the ad-hoc design of the process, such that the material is intentionally weakened in predetermined regions of different geometry through incomplete densification. This allows the fracture to be localised in priori-designed areas. The original method is applied to achieve local control of material densification by electron beam powder bed fusion (PBF-EB). A comparative study is used to verify the feasibility of the method in a variety of design configurations and to quantify the effect on mechanical properties as a first step toward a tunable mechanical response.

2 Materials and Methods

2.1 Specimens Design

The layer-by-layer production approach allows for local process control and is used in this work to modulate the construction in such a way [25] as to intentionally obtain incomplete densification of the material in a specific region of the component. Figure 1 shows an example of
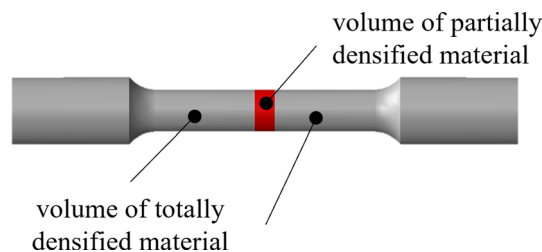

Fig. 1 Representation of the prepared samples

a representative sample where the red coloured portion corresponds to the volume that is only partially densified.

Different geometries and positions of the weakened area in a tensile specimen were fabricated and tested to investigate the feasibility of a predetermined fracture and the effect on the mechanical behaviour. The tensile specimens were designed according to UNI EN ISO 6892-1 with a gauge length of 45 mm.

Figure 2 shows a portion of the axial section of the axisymmetric cylindrical tensile specimens, displaying the weakened region embodied in the specimen geometry. In Fig. 2, G denotes half the thickness of the volume of the weakened area, measured perpendicularly to the surfaces. Figure 2a shows a flat geometry (F) located at the centre of the specimen gauge length and realised with a G of 0.050 and 0.100 mm for specimens F2 and F4, respectively. For this geometry, an additional set of specimens was produced with the weakened region 9 mm from the centre of the specimen. These samples were labelled F2.1 and F4.1, respectively. The sections from Fig. 2 b to e consist of two parts shaped as pin and tail, respectively. Figure 2b shows a hill-shaped (H) weakened volume. The G value was set to 0.050 and 0.100 mm, and the configurations were named H2 and H4, respectively. The shapes in Fig. 2 c, d, and f are a cone (P), a truncated cone (TC) whose top surface has a diameter of 1 mm and a plane inclined at 45 degrees (C). The G value for these shapes was equal to 0.050 mm.

For each shape, six replicas were fabricated using the Arcam A2X, an PBF-EB system. Before the melting phase, each layer was preheated at 700 °C. Standard Ti6Al4V powder was used with a powder size distribution ranging between 50 and 150 μm. The layer thickness was set equal to 0.050 mm, corresponding to the minimum G value. The total number of specimens was 42, plus 5 bulk specimens with no intentional defect used to measure the reference properties. All specimens were constructed with the axis parallel to the build direction. The samples were randomly positioned on the build plate and equally spaced to avoid any bias related to heat accumulation in specific zones of the build volume [26]. The process parameters for the fully densified and weakened sections are listed in Table 1.
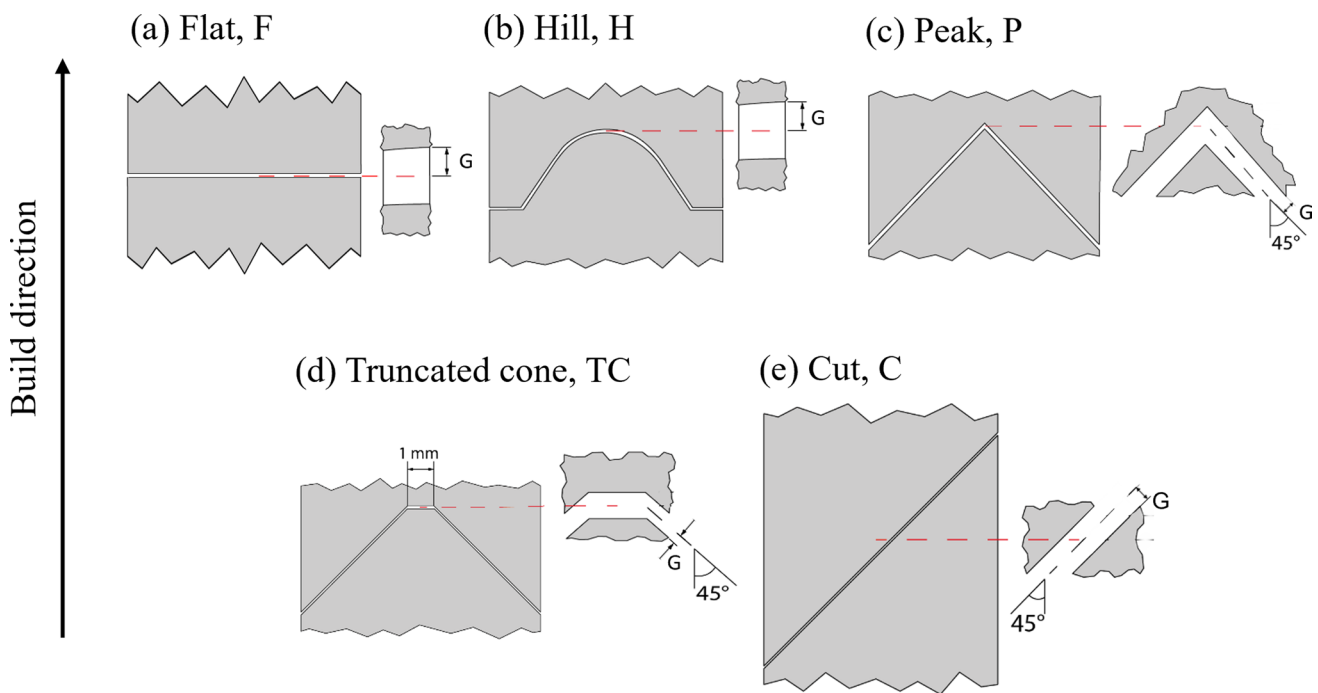
(a) Flat, F   **(b) Hill, H**   **(c) Peak, P**

(d) Truncated cone, TC   **(e) Cut, C**

Fig. 2 Shapes of the weakened volume embedded in tensile specimens

Table 1 Process parameters

		Scan speed [mm/s]	Focus Offset [mA]	Beam current [mA]	Number of contours	Line offset [mm]
Bulk (solid, dense volume)	Contour (mode MultiBeam)	850	5	6	3	0.25
	Hatching	1754	25	12	-	0.2
Weakened volume	Hatching	10,000	45	48	-	0.5

After fabrication, a replica of specimen F2 was inspected using computed tomography scanning (CT-scan) (GE Phoenix v|tome|x s). The scans were performed with the following parameters: voltage of 240 kV, current of 150 µA, and voxel size of 0.035 µm. In addition, all specimens were sectioned, polished, and viewed with a stereomicroscope.

The specimens were tested in the as-built condition, without any surface treatment on the gauge length. Surface roughness was measured using a Nikon LV 150 Confovis microscope under the following conditions: 10x microscopy objective, 0.5 µm vertical quantization, and scanned area of 2.4 mm × 1.0 mm. The acquired maps were processed as prescribed in ISO 25178-603:2013 to determine the average areal roughness S_a of the S-L surface after removing the cylindrical shape and linear Gaussian filtering with a cut-off of 0.8 mm.

Then, three replicas were tested at room temperature under tensile load at a 0.5 mm/min speed in a Zwick Z050 machine with a 50kN load cell. The deformation was recorded with a laser extensometer.

3 Results and Discussion

An example of the samples produced (a replica of specimen F) is shown in Fig. 3. The integrity of the outer surface of the specimen in the as-built condition can be observed in Fig. 3a, where the flat weakened area is not visible. The continuity of the external surface is also confirmed by the 3D reconstruction of tomography analysis (Fig. 3b). Figure 3c shows a section from the CT scan of the weakened volume, where the expected incomplete densification is confirmed (Fig. 3c). An annular region can be seen at the edge where the material appears denser than in the core. The higher densification at the slice boundary could be caused by deeper penetration of the energy beam as it melts the contour of the layers above the defect or by a skin effect due to heat

Fig. 3 **a** Picture of the as-built specimen F2; **b** X-ray CT Scan 3D reconstruction of the central portion of as-built Specimen F2, in which the weakened volume is located; **c** cross-section of the as-built specimen F2 in the centre of the weakened volume extracted from CT Scan, **d** surface map (S-L surface) measured by confocal profilometry
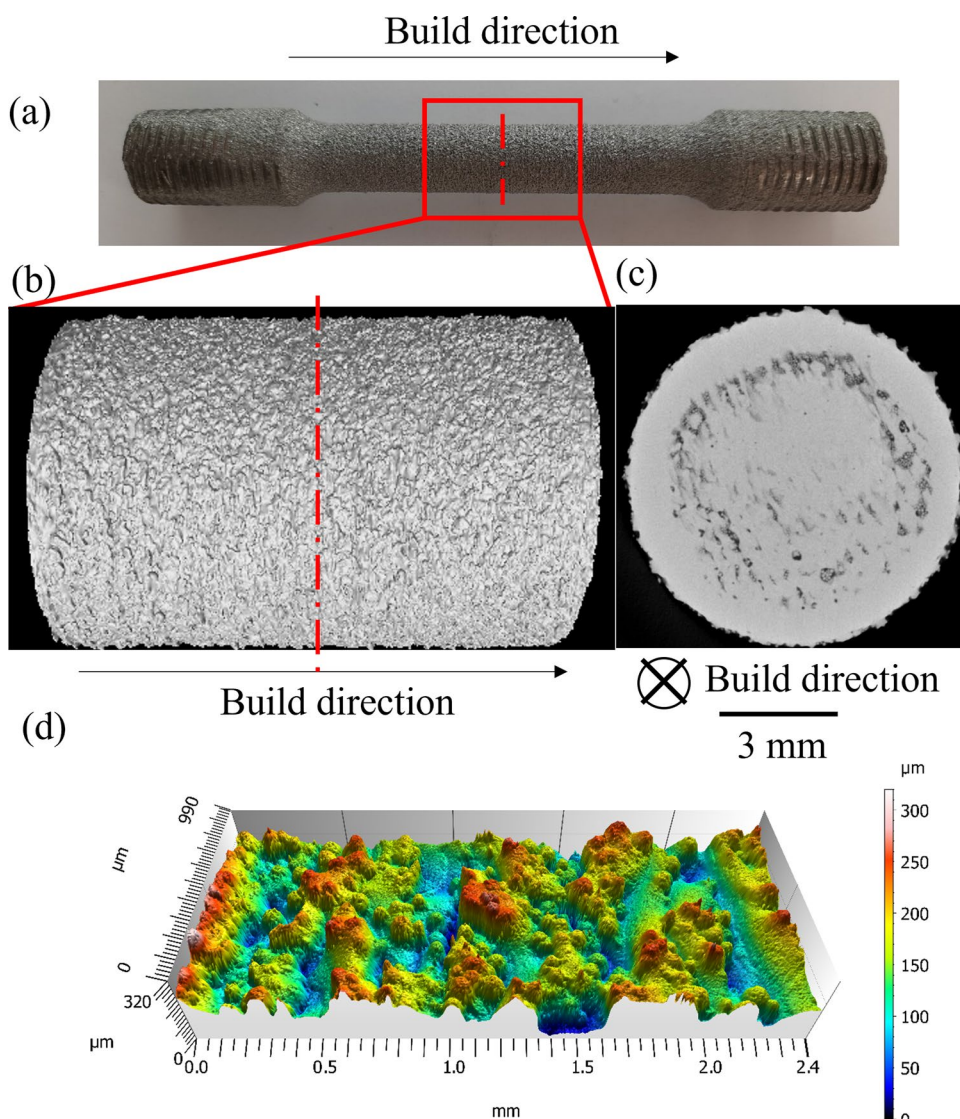
transfer from the lower and upper bulk regions which cannot be dissipated through the surrounding material [26]. In fact, in the upskin surfaces produced by PBF-EB, heat accumulation is often observed at the edge of each slice because the conductivity of the surrounding unmelted powder is lower than the solidified material [26].

Figure 3d shows the S-L surface map measured by confocal profilometry: S_a values resulted in 39 μm, accordingly to the literature [26].

Figure 4 shows microscopic images of polished axial sections of weakened specimens. As can be observed, the weakened region is well recognisable with respect to the bulk material. Higher magnification shows segments consisting of only slightly sintered particles, confirming proper tuning of process parameters that do not cause full melting.

For completeness, the experimental values of G were measured on the images of the cross-section of all samples and reported in Fig. 4. As observed, the G values obtained

are always higher than the corresponding nominal counterpart. In particular, except for sample F4, the G value is about double the nominal one. This is explained considering that, to account for the consolidation of the powder during the melting phase, the deposited amount of powder is always greater than the established layer [27]. Since the material in the weakened regions is not fully melted, the final layer thickness results higher and, correspondingly, the G value. This finding is not evident for samples F2 and F4 because a portion of the expected powder shrinkage [28] is compensated by the energy provided when melting the subsequent layers. In fact, it can be noticed that, for a given G value, when the geometry is horizontal or approaching horizontal orientation, the weakened zone is less marked than for inclined segments. This phenomenon is particularly evident in sample H4 where the G value is nominally 0.1 mm, resulting in a fading defect at the top of the hill and the horizontal outer regions, while the weakened portion is pronounced
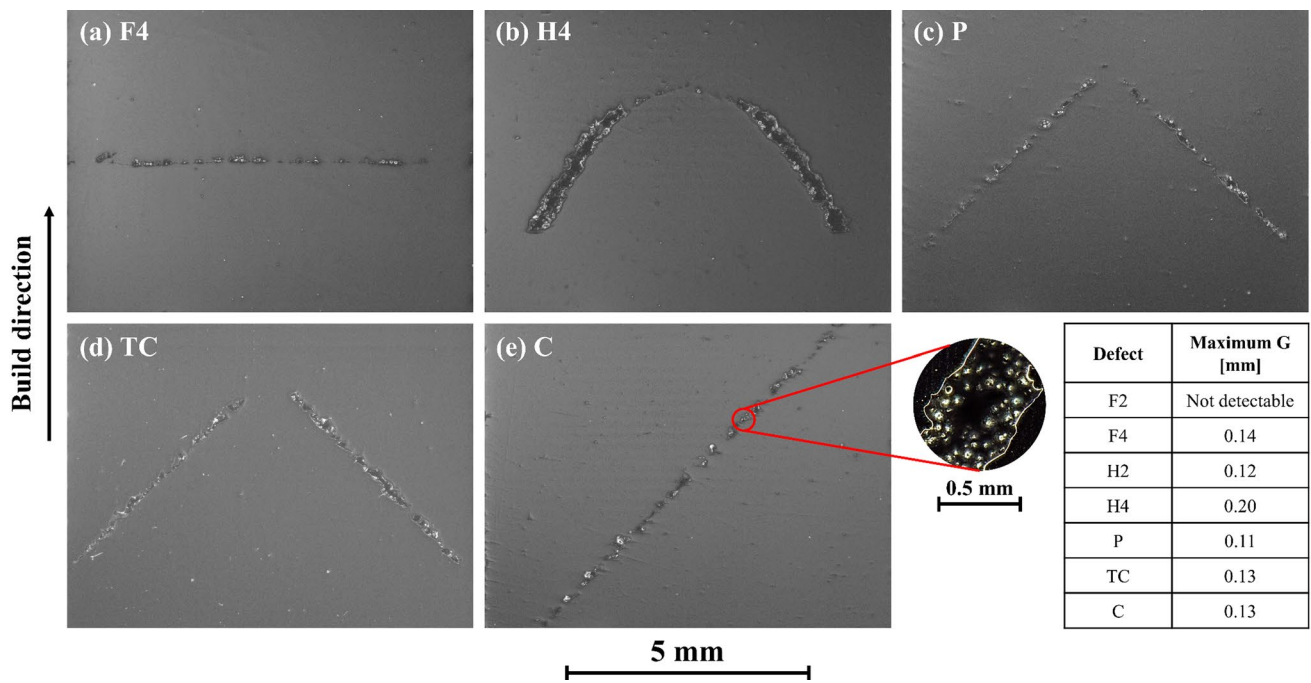
Fig. 4 Stereomicroscope images of the axial section for each geometry
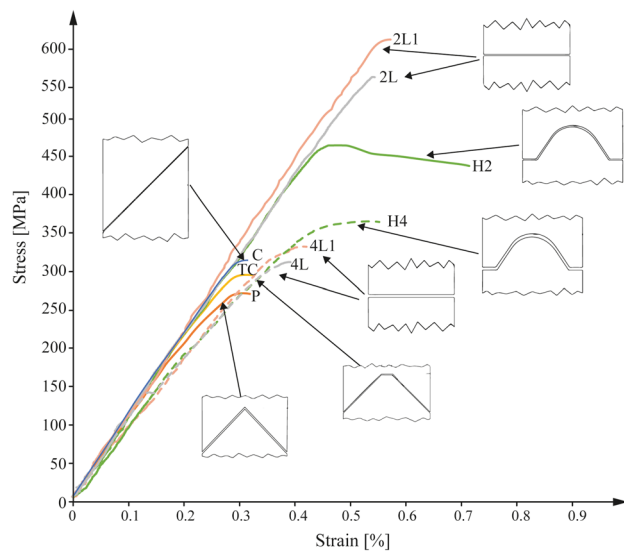

Fig. 5 Comparison of strain-stress curves for different geometries of the weakened volumes

where the slope is steeper. Similar considerations explain the result for the flat shape F4 with nominal G of 0.1 mm and the inclined geometries in P, TC and C with G equal to 0.05 mm.

The tensile behaviour of a representative specimen for each geometry is shown in Fig. 5. The resulting values of the tensile properties are listed in Table 2, which gives the average and deviation over the three tests. Table 2 also lists the mechanical properties of the bulk specimens. Stresses

were determined using the area of the nominal cross-section of the specimens, disregarding the presence of intentional defects. Therefore, the maximum force is also provided for a more precise comparison. In addition, the tensile strength and maximum strain were normalised with respect to the values of the bulk specimens. An example of each pin and tail specimen geometry after the tensile test is provided in Fig. 6. The fractured bits shown are those built closer to the build platform. In all cases, the fracture has occurred within the weakened area and is shaped as it was designed. Figure 7 shows SEM images of the fracture surfaces of specimens F2 and F4: the bottom surfaces (Fig. 7a and c) are those that were built as upskin surfaces during construction, which means that the build direction Z is pointing out of the images. The top surfaces (Fig. 7b and d), on the other hand, are the counterparts on the side of the material built on top of the weakened layers.

As for the mechanical properties, the low deviation for all measured quantities proves the repeatability of the process in all cases, even in the presence of such macroscopic defects as the designed weakened volumes. Within the deviation values, the Young modulus of the weakened structures is comparable to that of the bulk material, especially for the flat shape. As desired, the tensile strength and the maximum strain differ significantly from the bulk material and among the geometries. Remarkably, the flat shapes with the lowest G had the highest strength value, with a maximum corresponding to about 70% of the bulk material. The other geometries exhibited much lower strength, especially geometries

Table 2 Comparison of tensile properties. The superscript n indicates the normalised value with respect to the bulk properties. E is the Young's modulus, R_m the tensile strength, F_{max} the maximum load, ε_{max} the strain at break

	E (St. dev) [MPa]	R_m (St. dev) [MPa]	R_m^n (St. dev) [MPa]	F_{max} (St. dev) [kN]	ε_{max} (St. dev) [%]	ε_{max}^n (St. dev) [%]
Bulk	110 (5)	887 (55)	-	59.10 (3.66)	5.2 (0.5)	-
F2	110 (3)	606 (74)	0.683 (0.083)	38.86 (4.08)	0.6 (0.1)	0.106 (0.014)
F4	110 (6)	338 (24)	0.381 (0.027)	21.54 (1.45)	0.4 (0.1)	0.083 (0.011)
F2.1	112 (1)	626 (32)	0.705 (0.036)	40.14 (1.39)	0.6 (0.0)	0.115 (0.000)
F4.1	88 (0)	331 (1)	0.373 (0.002)	21.13 (0.28)	0.4 (0.0)	0.077 (0.000)
H2	104 (3)	452 (27)	0.510 (0.031)	29.74 (1.54)	0.7 (0.1)	0.131 (0.016)
H4	97 (3)	363 (7)	0.409 (0.008)	23.69 (0.42)	0.5 (0.0)	0.105 (0.001)
C	109 (2)	328 (99)	0.369 (0.112)	21.63 (6.49)	0.3 (0.1)	0.064 (0.015)
P	101 (1)	271 (10)	0.305 (0.011)	17.54 (0.48)	0.3 (0.0)	0.064 (0.003)
TC	103 (5)	314 (33)	0.354 (0.037)	20.59 (2.22)	0.4 (0.0)	0.068 (0.006)

Fig. 6 Surface fracture profiles of the samples: **a** flat tilted of 45 degrees, C, **b** conical shape, P, **c** truncated cone, TC, **d** and **e** hill-shapes, H2 and H4, respectively
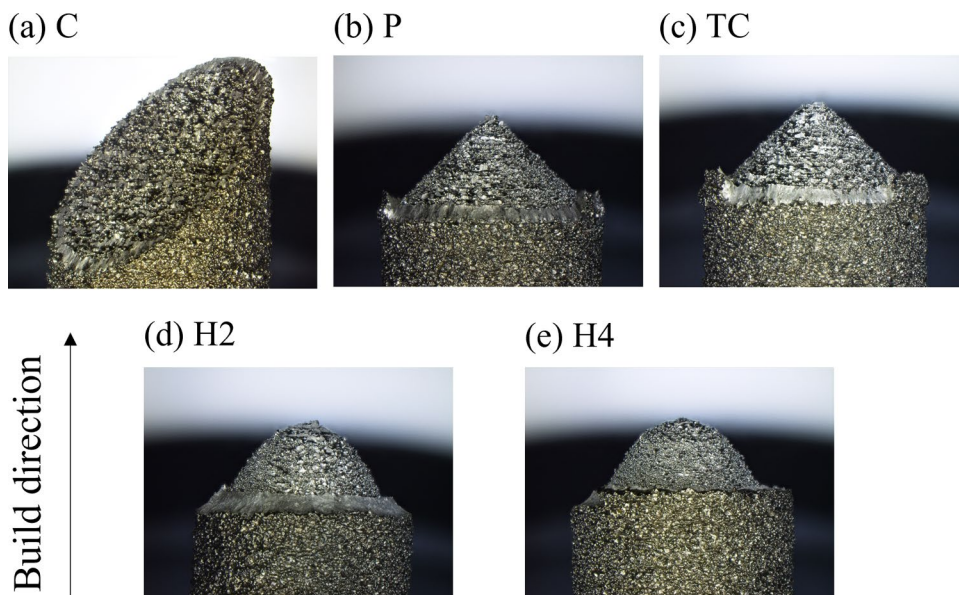
C, TC, and P. This behaviour can be explained by considering the fracture mechanisms in the weakened volume, which are related to the connections formed between the upper and lower bulk volumes through the weakened volume.

Figure 8 shows SEM images of the fracture surfaces to help interpret the results. It is important to remember that the method of obtaining the weakened volume involves the creation of an agglomeration of powder particles. Therefore, the flat weakened volume is formed by overlapping horizontal layers where the whole layer, or a portion, is only sintered. Practically, the sintering creates a connection, called neck, between the particles [29]. In addition to the energy provided to process the weakened layers, the melting of subsequent layers out of the weakened regions provides a supplementary heat flux. This extra energy strengthens the necks formed, especially along the build direction (which corresponds to

the loading direction) and may also be responsible for the formation of the annular region, whose thickness is approximately 550 μm (Fig. 8f). However, likely, the annular, denser rim (Fig. 8f) and the necks formed between the particles in the core region contribute separately to the tensile behaviour. In fact, each neck between two particles [29] could behave like a separate micro tensile specimen with a very short gauge length. However, owing to the large number of pores in the weakened volume, fracture occurs suddenly without plastic deformation. Fracture proceeds through the necks (Fig. 8c), which explains why powder particles adhere to the surfaces after rupture (Fig. 7). At higher magnification, the boundary between the dense outer rim and the weakened centre (Fig. 8b) shows the co-presence of the ductile failure by micro-voids coalescence of the fully-dense material (Fig. 8d), and smooth areas that were detached even before
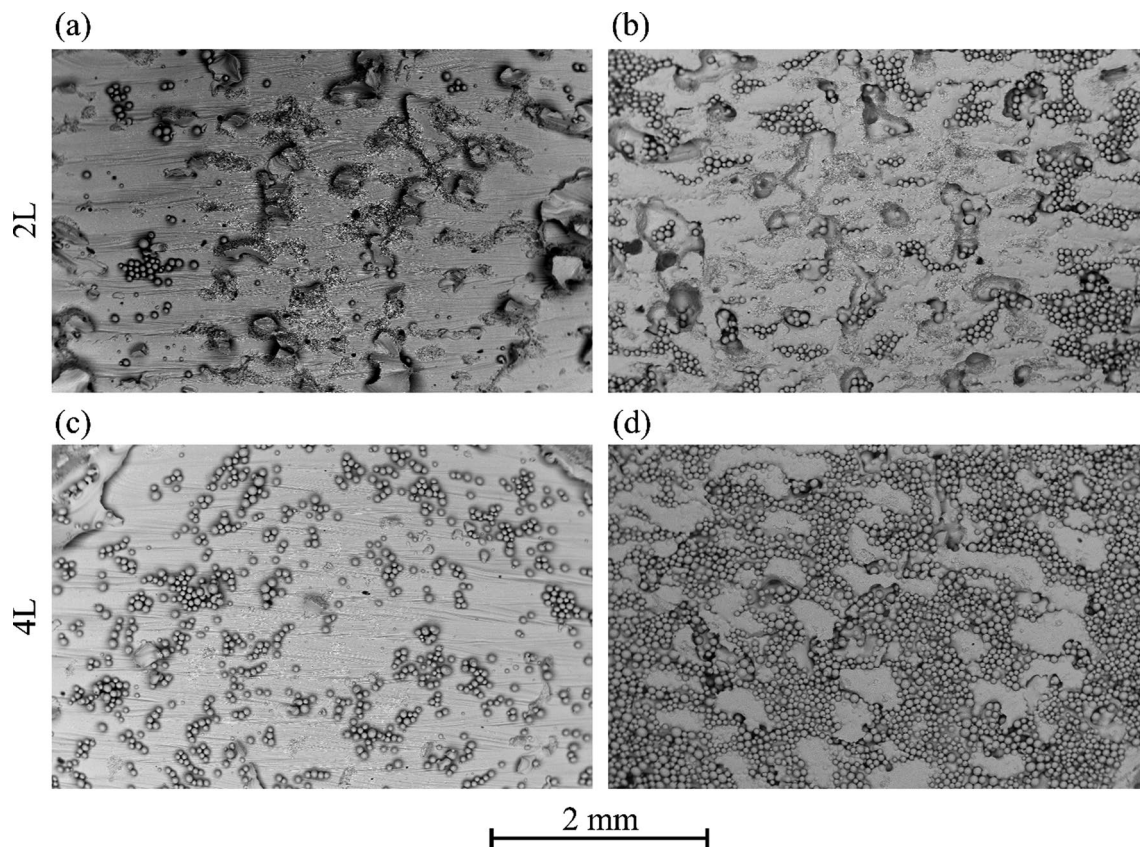
Fig. 7 SEM images of fracture surfaces of F samples: bottom surface (build direction Z points out of the images) of specimen **a** F2 and **c** F4; and top surface (build direction Z points into the images) of specimen **b** F2 and **d** F4

the test. Fracture in the stress-bearing areas has the same morphology as in the bulk specimen (Fig. 8a vs. d).

With the same G, the like pin and tails geometries showed lower strength. The result is consistent with the effective gap being almost half the nominal value for flat weakened regions, while it is just slightly below the expected value for inclined shapes (Fig. 4). This can be explained by considering that, in the non-flat shapes, the 3D development of the weakened regions may have facilitated heat dissipation [26], preventing the formation of stronger connections as in the case of flat shapes and leading to a result more in line with the design. Figure 9 shows a schematic diagram of the heat transfer occurring during the process at a specified layer. When the electron beam impacts the powder, and the kinetic energy is transformed into heat, the heat flows in all directions, but preferentially towards the material at lower heat resistance (higher conductivity). All the geometries are surrounded by powder that was weakly sintered by the preheating phase of the PBF-EB process. This powder has extremely poor conductivity with respect to the bulk material and therefore represents a barrier against heat transfer and a point of heat accumulation. As mentioned above, this explains the

observed annular region in Fig. 3c. In the case of the flat surface, the heat flows from the top surface of the weakened area through the weakened area toward the bulk substrate. Since the PBF-EB process occurs at a high temperature, above the sintering point of the powder material, and the weakened area has a low conductivity, the heat transfer occurs slowly, giving the time to reach stronger sintering, obtaining stronger connections between the particles. In the case of a 3D shape, one side of the weakened material is adjacent to the bulk material, and therefore the heat is rapidly transferred to the adjacent region toward the bulk material, which has higher conductivity. This fast transfer provokes a lower sintering degree and, therefore, a weaker connection between the particles. At a given layer, the larger the slide portion covered by the weakened area is, the slower the heat transfer and, therefore, stronger are the connection with the particles. This finding is also consistent with the fact that the smoother volumes (more gradual cross-sectional variation of the weakened volume) showed higher strength and higher strain when compared to more drastic shapes (e.g., H2 vs. P in Table 2). Specimens TC and C showed similar maximum strength and strain (Table 2). The H sample is more ductile and shows some,

Fig. 8 SEM images: **a** fracture surface of an as-built bulk specimen; **b** fracture surface of specimen F2 at the boundary between the weakened area and the dense annular region; **c** fracture surface at the centre of specimen F2 with the presence of unmelted particles attached to the surface; **d** magnification of detail in **b**; **e** fracture surface in a neck, **f** fracture surface of specimen F2 at the perimeter of the weakened volume
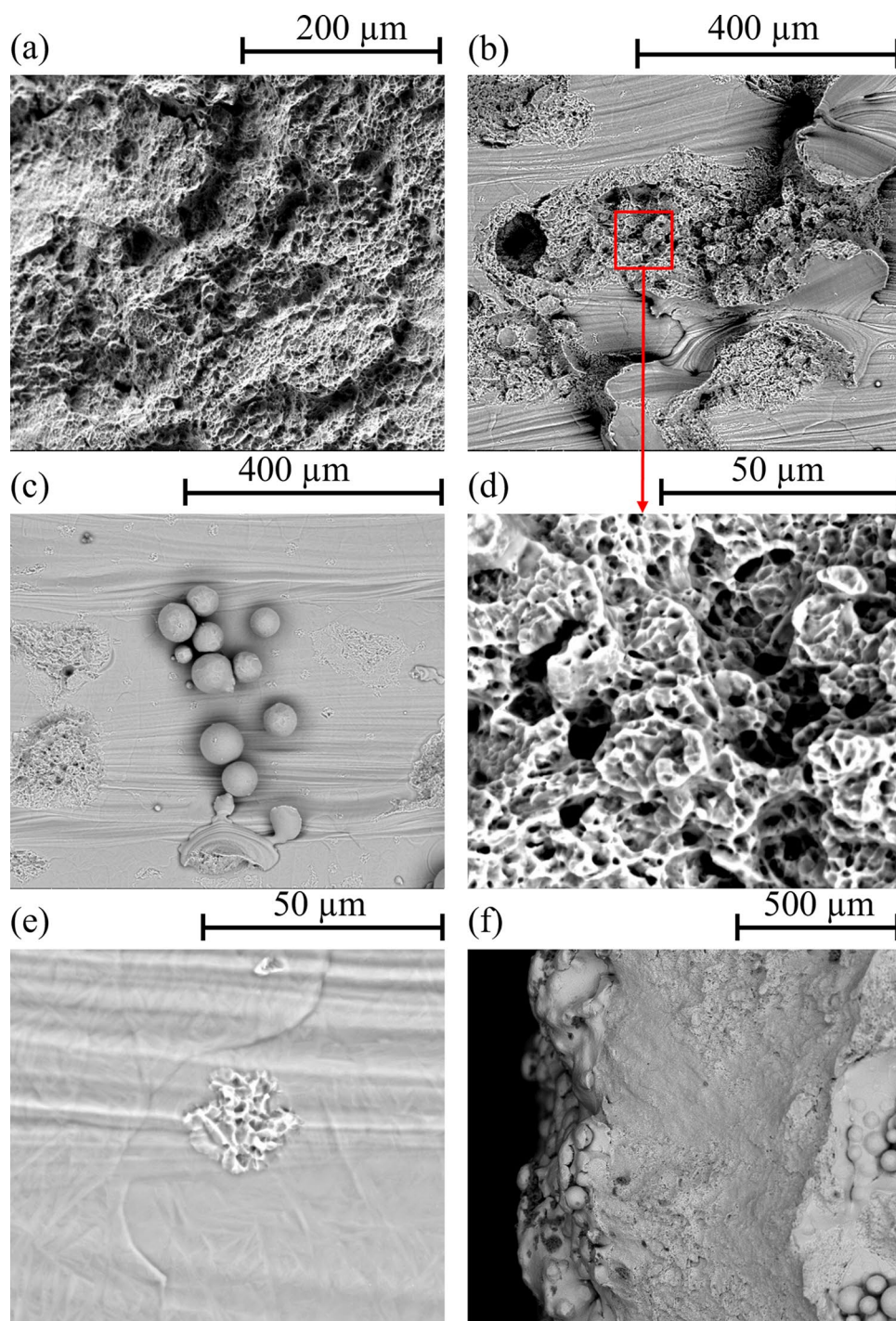
but very limited, plastic deformation. This could be due to the wider extension of the surface that is generated as the specimen break. In this case, defects with such a geometry promote fracture growth through the coalescence of micro-voids in the sintered volume and along the defect surfaces.

Comparing defects with the same shape but different volumes (i.e., different G values), a thicker volume will result in a weaker connection and, thus, lower maximum stress and strain (e.g., H2 versus H4 or F2 versus F4). In the case

of a flat shape, doubling the G-value (specimens F2 vs. F4) reduces the maximum stress by half.

4 Conclusions

In this work, the achievability of a controlled fracture was studied experimentally by designing the production process and the part accordingly. Intentionally weakened

Fig. 9 Heat trasfer mechanisms when producing **a** flat and **b** 3D weakened areas

(a) Flat shape

(b) 3D shape
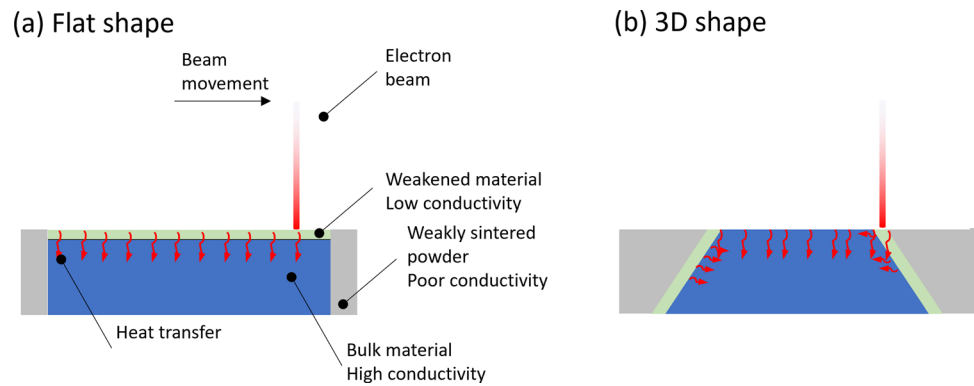
portions were embedded into specimens for designing a specific zone of fracture. Regions with lower density respect to the bulk material were considered as modifiers of the part properties. In this framework, weakened regions with specific geometries were embedded in a tensile specimen that serves as a dummy. Different geometries of the weakened volume were tested. The results confirmed the feasibility of the innovative method for predetermining the fracture surface and showed a preliminary qualitative correlation between the tensile response and the design of the weakened volume. Under the same process parameters, the fracture mode and the load response of the specimen can be related to the designed weakness. With the same thickness of the weakened volume, the 3D development of the weakened geometries turned into varying resistance due to heat transfer and accumulation during the PBF-EB process. The results also showed that with a proper geometry definition, it is possible to vary the extent of deformation before rupture for a given strength. The rapid evolution of the fracture could be exploited for devices that need to respond immediately to any overload. Shapes enabling a plastic behaviour, such as sample H, can instead be applied where it is useful to monitor the load achieved. Such programmable response of the component paves the way to devices that connect two or more parts of a complex system in compliant engagement and allows their separation when the load/strain is unsafe for the system (exceeds a predetermined value) without causing the system to fail. Similarly, this methodology could easily be extended to crack propagation control. In addition to mechanical properties, this concept can also be used to locally modify other material properties, such as electrical and thermal.

Declarations

References

1. K.V. Wong, A. Hernandez, A review of additive manufacturing. Int. Sch. Resh. Notices **2012**, 208760 (2012). https://doi.org/10.5402/2012/208760

2. H.Y. Wan, Z.J. Zhou, C.P. Li et al., Effect of scanning strategy on mechanical properties of selective laser melted Inconel 718. Mater. Sci. Eng. A **753**, 42 (2019). https://doi.org/10.1016/j.msea.2019.03.007

3. R.R. Dehoff, M.M. Kirka, F.A. List, K.A. Unocic, W.J. Sames, Crystallographic texture engineering through novel melt strategies via electron beam melting: Inconel 718. Mater. Sci. Technol. **31**, 939 (2015). https://doi.org/10.1179/1743284714Y.0000000697

4. K. Sanjeeviprakash, A.R. Kannan, N.S. Shanmugam, Additive manufacturing of metal-based functionally graded materials: overview, recent advancements and challenges. J. Brazilian Soc. Mech. Sci. Eng. **45**, 241 (2023). https://doi.org/10.1007/s40430-023-04174-1

5. A. Müller, G. Schlick, R. Neu, C. Anstätt, T. Klimkait, J. Lee, B. Pascher, M. Schmitt, C. Seidel, Additive manufacturing of pure tungsten by means of selective laser beam melting with substrate preheating temperatures up to 1000 °C. Nucl. Mater. Energy **19**, 184 (2019). https://doi.org/10.1016/j.nme.2019.02.034

6. T. Zhang, Z. Huang, T. Yang, H. Kong, J. Luan, A. Wang, D. Wang, W. Kuo, Y. Wang, C.-T. Liu, In situ design of advanced titanium alloy with concentration modulations by additive

manufacturing. Science **374**, 478 (2021). https://doi.org/10.1126/science.abj3770

7. G.M. Karthik, H.S. Kim, Heterogeneous aspects of additive manufactured metallic parts: a review. Met. Mater. Int. **27**, 1 (2021). https://doi.org/10.1007/s12540-020-00931-2

8. A. Azarniya, X.G. Colera, M.J. Mirzaali, S. Sovizi, F. Bartolomeu, M.St Weglowski, W.W. Wits, C.Y. Yap, J. Ahn, G. Miranda, F.S. Silva, H.R.M. Hosseini, S. Ramakrishna, A.A. Zadpoor, Additive manufacturing of Ti–6Al–4V parts through laser metal deposition (LMD): process, microstructure, and mechanical properties. J. Alloys Compd. **804**, 163 (2019). https://doi.org/10.1016/j.jallcom.2019.04.255

9. N. Raghavan, S. Simunovic, R. Dehoff, A. Plotkowski, J. Turner, M. Kirka, S. Babu, Localized melt-scan strategy for site specific control of grain size and primary dendrite arm spacing in electron beam additive manufacturing. Acta Mater. **140**, 375 (2017). https://doi.org/10.1016/j.actamat.2017.08.038

10. A. Plotkowski, J. Ferguson, B. Stump, W. Halsey, V. Paquit, C. Joslin, S.S. Babu, A. Marquez Rossy, M.M. Kirka, R.R. Dehoff, A stochastic scan strategy for grain structure control in complex geometries using electron beam powder bed fusion. Addit. Manuf. **46**, 102092 (2021). https://doi.org/10.1016/J.ADDMA.2021.102092

11. D. Bürger, A.B. Parsa, M. Ramsperger, C. Körner, G. Eggeler, Creep properties of single crystal Ni-base superalloys (SX): a comparison between conventionally cast and additive manufactured CMSX-4 materials. Mater. Sci. Eng. A **762**, 138098 (2019). https://doi.org/10.1016/j.msea.2019.138098

12. L.S. Dimas, M.J. Buehler, Modeling and additive manufacturing of bio-inspired composites with tunable fracture mechanical properties. Soft Matter **10**, 4436 (2014). https://doi.org/10.1039/c3sm52890a

13. G.D. Guercio, M. Galati, A. Saboori, P. Fino, L. Iuliano, Microstructure and mechanical performance of Ti–6Al–4V lattice structures manufactured via Electron Beam Melting (EBM): a review. Acta Metall. Sin. (Engl. Lett.) **33**, 183 (2020). https://doi.org/10.1007/s40195-020-00998-1

14. S. Mantovani, M. Giacalone, A. Merulla, E. Bassoli, S. Defanti, Effective mechanical properties of AlSi7Mg additively manufactured cubic lattice structures. 3D Print. Addit. Manuf. **9**, 326 (2022). https://doi.org/10.1089/3dp.2021.0176

15. M. Galati, M. Giordano, L. Iuliano, Process-aware optimisation of lattice structure by electron beam powder bed fusion. Prog Addit. Manuf. **8**, 477 (2023). https://doi.org/10.1007/s40964-022-00339-x

16. M. Patel, A. Aggarwal, A. Kumar, Investigation of cracking susceptibility and porosity formation and its mitigation techniques in laser powder Bed Fusion of Al 7075 alloy. Met. Mater. Int. **29**, 2358 (2023). https://doi.org/10.1007/s12540-023-01387-w

17. S.-Y. Min, Y. Kim, T.K. Lee, S. Seo, H.S. Jung, D. Kim, J. Lee, B.-J. Lee, The effect of porosity on the elasticity of pure titanium: an atomistic simulation. Met. Mater. Int. **16**, 421 (2010). https://doi.org/10.1007/s12540-010-0612-8

18. J. Yang, Z. Fu, J. Ye, J. Ye, D. Kübrich, C. Körner, Electron beam-based additive manufacturing of Fe93.5Si6.5 (wt.%) soft magnetic material with controllable magnetic performance. Scr. Mater. **210**, 114460 (2022). https://doi.org/10.1016/j.scriptamat.2021.114460

19. A.Y. Kumar, J. Wang, Y. Bai, S.T. Huxtable, C.B. Williams, Impacts of process-induced porosity on material properties of copper made by binder jetting additive manufacturing. Mater. Des. **182**, 108001 (2019). https://doi.org/10.1016/j.matdes.2019.108001

20. N.L. Pedersen, Designing plates for minimum internal resonances. Struct. Multidiscip. Optim. **30**, 297 (2005). https://doi.org/10.1007/s00158-005-0529-x

21. C. Maucher, H. Teich, H.C. Möhring, Improving machinability of additively manufactured components with selectively weakened material. Prod. Eng. **15**, 535 (2021). https://doi.org/10.1007/s11740-021-01038-2

22. L. Jiang, W. He, B. Wei, Z. Wang, S. Li, The shear pin strength of friction pendulum bearings (FPB) in simply supported railway bridges. Bull. Earthq. Eng. **17**, 6109 (2019). https://doi.org/10.1007/s10518-019-00698-x

23. S.P. Rabiei, R. Azarafza, Investigate of mechanical fuse in Cardan Shaft using FEM. Rev. Inf. Eng. Appl. **1**, 1 (2014). https://doi.org/10.18488/journal.79/2014.1.1/79.1.1.10

24. A. Souto, J. Zhang, A.M. Aragón, K.P. Velikov, C. Coulais, Edible mechanical metamaterials with designed fracture for mouthfeel control. Soft Matter **18**, 2910 (2022). https://doi.org/10.1039/d1sm01761f

25. M. Galati, E. Bassoli, A. Gatto, L. Iuliano, Additive manufacturing process and product obtainable through the process, Patent No. WO2022259196A1 (2022)

26. M. Galati, G. Rizza, S. Defanti, L. Denti, Surface roughness prediction model for electron beam melting (EBM) processing Ti6Al4V. Precis. Eng. **69**, 19 (2021). https://doi.org/10.1016/j.precisioneng.2021.01.002

27. M. Galati, Electron beam melting process: a general overview, in *Additive Manufacturing Handbooks in Advanced Manufacturing*, ed. by J. Pou, A. Riveiro, J. Paulo Davim (Elsevier, Amsterdam, 2021) pp. 277–301. https://doi.org/10.1016/B978-0-12-818411-0.00014-8

28. M. Galati, A. Snis, L. Iuliano, Powder bed properties modelling and 3D thermo-mechanical simulation of the additive manufacturing Electron Beam melting process. Addit. Manuf. **30**, 100897 (2019). https://doi.org/10.1016/j.addma.2019.100897

29. G. Rizza, M. Galati, L. Iuliano, A phase-field study of neck growth in electron beam powder bed fusion (EB-PBF) process of Ti6Al4V powders under different processing conditions. Int. J. Adv. Manuf. Technol. **123**, 855 (2022). https://doi.org/10.1007/s00170-022-10204-4